J Nanopart Res (2020) 22: 45
https://doi.org/10.1007/s11051-020-4759-z

RESEARCH PAPER

The particle size effect of $Yb_{0.8}R_{0.2}MnO_3$ (R is Sm, Nd, and Eu) on some physical properties

I. A. Abdel-Latif

Received: 18 December 2019 / Accepted: 22 January 2020 / Published online: 6 February 2020

Abstract $YbMnO_3$ as a rare earth manganite class of perovskite materials displayed a wide range of applications and interests for scientists. This hexagonal perovskite showed a simultaneous ferromagnetism, ferroelectricity, and ferroelasticity properties, which is considered multiferroic materials. This unique magnetic property may lead to use them in spintronic and magnetic storage media. $YbMnO_3$ and $Yb_{0.8}R_{0.2}MnO_3$ are prepared with different particle sizes to study the effect of its difference in particle size on the electrical properties and Raman scattering. All samples are prepared using co-precipitation method from the initial pure chlorides of ytterbium, samarium, europium, and manganese to be reacted with pure sodium hydroxide taking into consideration the suitable molar ratio. The EDS spectra confirmed the existence of each element in the proposed compounds according to the suggested structure. The hexagonal crystal system of space group $P6_3cm$ (185) is found for all samples. From the experimental Raman measurements, the observed lines in spectra of $Yb_{0.8}Nd_{0.2}MnO_3$ are found at 102, 131, 212, 460, 631, and 685 cm^{-1}, and lines in spectra of $Yb_{0.8}Sm_{0.2}MnO_3$ are found at 101, 137, 217, 462, 630, and 687 cm^{-1}, which correspond to E_2, A_1, E_2, A_1, E_1, and A_1, respectively. The obtained materials showed semiconducting behavior with different activation energy gap (E_a of the undoped ytterbium manganite, $E_a = 0.255$ eV, increased because of doping to be 414 and 447 eV for Nd- and Sm-doped samples, respectively). The complex impedance measurements are strongly related to the microstructure of polycrystalline materials and depend on the grain size. Our electrical properties enhance the hopping mechanism of charge carrier's transfer in the under investigation samples. The significant difference in activation energy between pure and doped ytterbium manganites were found because of the remarkable difference in the crystalline size. The crystalline size observed for pure ytterbium manganite is 67 nm to be increased with doping.

Keywords Ytterbium manganites · Hexagonal perovskites · Dielectric properties · Raman spectra · Nano-crystalline

This article is part of the topical collection: Nanotechnology in Arab Countries

Guest Editor: Sherif El-Eskandarany

I. A. Abdel-Latif (✉)
Physics Department, College of Science and Arts, Najran University, King Abdul Aziz Road, P.O. 1988, Najran, Saudi Arabia
e-mail: ihab_abdellatif@yahoo.co.uk

I. A. Abdel-Latif
Advanced Materials and Nano-Research Centre, Najran University, P.O. Box: 1988, Najran 11001, Saudi Arabia

I. A. Abdel-Latif
Reactor Physics Department, Nuclear Research Center, Atomic Energy Authority, Abou Zabaal, P.O 13759, Cairo, Egypt

Introduction

Rare earth manganites are wide class of materials, which have very rich properties and promising applications.

These interests excite scientists to study these unique and unusual phenomena hoping to find interpretations for these properties and new applications. The recent progress in rare earth manganite oxides having perovskites-like structure (Lee et al. 2008; Rossli et al. 2005**;** Bashkirov et al. 2003) reflects the extent of interest in basic and applied research devoted to these materials. These materials have very interesting chemical properties that may lead to apply them as chemical sensors, (Abdel-Latif et al. 2018a, b; Shuk and Guth 1995; Shuk et al. 1993), photocatalytic materials (Abdel-Latif et al. 2019; Abdel-Latif et al. 2017; Kanhere and Chen 2014). The unique magnetic and electrical properties such as magnetoresistance (Bashkirov et al. 2005; Abdel-Latif et al. 2008; Bouziane et al. 2005), magnetocaloric effect (Bettaibi et al. 2016; Gamzatov et al. 2017; Abdel-Latif et al. 2018a, b), and multiferroics properties (Lee et al. 2005; Fabreges et al. 2009; Ramesh and Spaldin 2007) increased the scientific interests of these materials and open the door to use these materials in magnetic devices, (Zhang et al. 2016*;* Das et al. 2014; Abdel-Latif et al. 2016*),* magnetic cooling (Ayas et al. 2017; Chandran et al. 2019; Cherif et al. 2014), and magnetic storage media and symmetries (cubic, orthorhombic, rhombohedral, monoclinic, and hexagonal structure), and this is one of the main reasons for the rich properties of these materials (Tokunaga et al. 2006; Mahato Dev et al. 2016; Elghoul et al. 2018). Rare earth manganites are formed with different crystal systems (Iqbal et al. 2017, Yousif et al. 2011; Parfenov et al. 2003, 2007; Markovich et al. 2013; Abdel-Latif et al. 2015; Maignan et al. 1997; Ritter 1996; Salama et al. 2008; Talbayev et al. 2008: Abdel-Latif 2011). The type of crystal structure formed depends on the annealing process and the ionic radius of the selected rare earth. The orthorhombic structures – rare earth manganites class of materials – exhibit the colossal magnetoresistance due to hole doping. Another complicated class related to the magnetic ordering in these materials of RMnO3 (R = Dy-Gd) is the ferroelectric or antiferroelectric induced by this magnetic ordering [39]. Another stable group of smaller ionic size compounds (R = Ho–Lu) have the hexagonal structure with *P63cm* space group showed the multiferroic properties (Wang et al. 2013; Zhou et al. 2006). Hexagonal structure family of these materials showed very interesting magnetic and dielectric properties. This hexagonal structure consists of MnO_5 bipyramids, where the nonequivalent O(3) and O(4) atoms forming triangular base and the O(1) and O(2) are located at the vertex (Iliev et al. 1997). The bonds originated from both manganese and oxygen atoms are as follows: Mn–O(1) and Mn–O(2) are slightly tilted with respect to the *c* axis. Raman spectra was used to describe the bond occurred between atoms and the type of motion represented (Smolenskii and Chupis 1981; Rousseau et al. 1981; Van Aken et al. 2004).

The dielectric loss factor is a very important factor. It is affected by the following parameters: electric conduction and various polarization mechanisms (including dipole, electronic, ionic, and Maxwell–Wagner) (Komarov et al. 2005). It is known that the formation of grain boundaries in the material occurred as a result of the annealing process that plays an important role in the oxidation and crystallization and reducing the surface area (Iqbal et al. 2012). The low conductivity is caused by the grain boundaries at low frequency that makes the contribution of grain boundaries pronounced in the relation between the dielectric constant and frequency (Naseem et al. 2018).

In this work, $YbMnO_3$ and $Yb_{0.8}R_{0.2}MnO_3$ (Nd and Sm) are prepared using a chemical method and annealed at different temperatures in order to get different particle sizes. Furthermore, it was studied the effect this difference in particle size on the Raman scattering, electrical, and dielectric properties.

Experimental details

The under investigation $YbMnO_3$, $Yb_{0.8}Sm_{0.2}MnO_3$, and $Yb_{0.8}Nd_{0.2}MnO_3$ samples were synthesized using co-precipitation method. Highly pure chloride solutions of $YbCl_3.6H_2O$, $SmCl_3.6H_2O$, $NdCl_3.6H_2O$, and $MnCl_2.4H_2O$ are mixed with NaOH solution with the proper molar ratios to be stirred for 6 h at temperature of 85 °C and in pH of 12. According to this method, the precipitated powders were washed many times, until getting rid of NaCl, and after that the produced powder of $YbMnO_3$, $Yb_{0.8}Sm_{0.2}MnO_3$, and $Yb_{0.8}Nd_{0.2}MnO_3$ are separated. Then, these powders are milled and pressed into a disc form of 10 mm diameter in order to start the annealing process. The pressed powder in discs form was heated at different temperatures, 750, 850, 950, and 1000 °C, in air for 12 h. The XRD patterns were collected using Cu radiation of 1.54 Å wavelength taken from PANalytical X'pert Pro MPR diffractometer. The Raman spectra were measured using (PerkinElmer) Raman spectrometer in the wave number range from

3000 up to 60 cm^{-1} with resolution of 4 cm^{-1}. The DC resistivity was measured as a function of temperature (from room temperature up to 573 K) using two- and four-point probe technique (Scientific Equipment & Services).The dielectric characteristics and AC conductivity were measured as a function of temperature and frequency (LCR) meter (HP4284A).

Results and discussions

As it is well-known, the rare earth manganite oxides crystalize in the form of perovskites. This perovskite-like structure has different crystal system forms, starting from simple cubic and transforming to some crystal systems such as the orthorhombic, the rhombohedral, the hexagonal, or the monoclinic system depending on the mechanism and method used for synthesis as well as the annealing and heat treatment process. The different crystal systems that perovskites reflect the wide range of interests are correlated with each structure and phase transition. The EDS test of all samples carried out and approved the forming of the required formula with the right elements ratio.

XRD structure analysis

In this work, the measured XRD patterns of $YbMnO_3$, $Yb_{0.8}Nd_{0.2}MnO_3$, and $Yb_{0.8}Sm_{.2}MnO_3$ at room temperature and from angle $2\theta = 10°$ up to 90° are shown in Fig. 1. It is quite clear that all samples have hexagonal crystal structure. All the peaks are indexed, and they satisfy this hexagonal crystal system of space group (P_{63cm}).

Not all miller indices are shown in Fig. 1, only up to (300) corresponding to $2\theta = 52.366°$ and $d = 1.7458$ Å because the existence of so many planes. Our indexed peaks are in good agreement with what was reported before (Talbayev et al. 2008; Abdel-Latif 2011; Bykov et al. 2019); the fitted of experimental XRD patterns based on Rietveld refinement was achieved using FullProf package software (Rodriguez-Carvajal 1993). The calculated parameters from the refinements such as lattice parameters, unit cell volume, and bond lengths of all samples are listed in Table 1. It is quite clear that the lattice parameter a of ytterbium manganite increased with doping as well as the unit cell volume V. Lattice parameter a increased because of Nd and Sm doping (from $a = 6.081$ Å up to $a = 6.09$ Å), while unit cell volume are closed $V = 365.5$ $Å^3$ of Nd doping and $V = 364.28$ $Å^3$ of Sm doping. The bond lengths between Yb–O and Mn–O bonds are given in Table 1. Comparing the values of the bond lengths of pure ytterbium manganite and doped ytterbium manganite, one can note the difference resulting from doping which may effect in the magnetic and electrical properties.

The crystalline size is one of the important parameters that play a role in the physical property dependence. It is calculated in this work from XRD patterns according to the well-known Scherrer formula (Abdel-Latif 2011).

$$\text{Crystalline size} = k\lambda/(B\sin\theta)$$

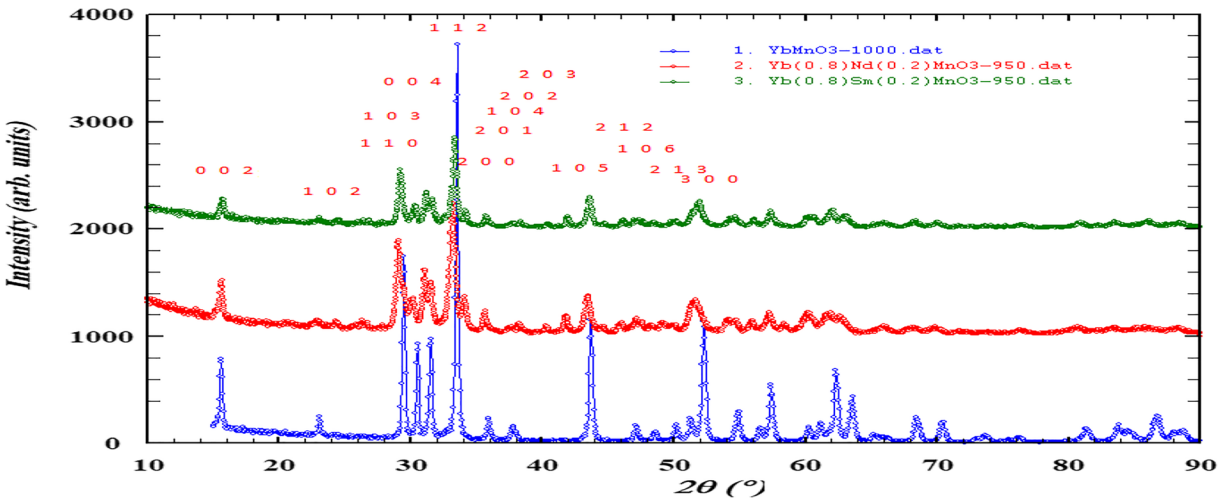

Fig. 1 XRD partners of YbMnO3, $Yb_{0.8}Nd_{0.2}MnO_3$, and $Yb_{0.8}Sm_{.2}MnO_3$ at room temperature

Table 1 Lattice parameters, unit cell volume, bond lengths, crystalline size, and activation energy of $YbMnO_3$, $Yb_{0.8}Nd_{0.2}MnO_3$, and $Yb_{0.8}Sm_{.2}MnO_3$

Compound	*a (Å)*	*c(Å)*	*V (Å^3)*	Bond lengths *(Å)*	Crystalline size *(nm)*	E_a *(eV)*
$YbMnO_3$	6.048(1)	11.340 (1)	359.27(0.1)	Yb1-O2 2.53(15) Yb2-O2 2.42(7) M1-O1 2.73(17) Mn2-O2 2.92(9) Mn2-O1 2.9(2)	750 ⇒ 67 1000 ⇒ 111	0.255
$Yb_{0.8}Nd_{0.2}MnO_3$	6.081(3)	11.414 (2)	365.54 (0.1)	Yb1-O2 2.58(14) Yb2-O2 2.23(7) M1-O1 2.64(12) Mn2-O2 2.64(9) Mn2-O1 2.69(12)	850 ⇒ 360 950 ⇒ 737	0.414
$Yb_{0.8}Sm_{.2}MnO_3$	6.090(4)	11.341 (5)	364.28(0.3)	Yb1-O2 2.5(5) Yb2-O2 2.4(2) M1-O1 2.99(16) Mn2-O2 2.6(3) Mn2-O1 2.6(4)	850 ⇒ 358 950 ⇒ 444	0.447

where B is equal to B_{obs}.-B_{std}. (B_{obs}. is FWHM of the observed sample and B_{std} is FWHM of the standard sample). The calculated values of the crystalline size for undoped and Nd-Sm-doped ytterbium manganites are listed in Table 1.

The crystalline size ranges from 67 nm for pure ytterbium manganites annealed at 750 C up to 111 nm after annealing at 1000 C. For the low temperature annealing of the doped ytterbium samples, the structure is not completely formed and it is formed at 750 °C. The crystalline size of doped samples and annealed at 850C are closed 360 and 358 nm. The 3-dimensional hexagonal unit cell representation was carried out using Diamond software for $YbMnO_3$, $Yb_{0.8}Nd_{0.2}MnO_3$, and $Yb_{0.8}Sm_{.2}MnO_3$ shown in Scheme 1.

Electron density $\rho(r)$ calculated from the scattering occurred when the X-ray incident on the unit cell. Fourier method is applied and the subprogram in FullProf package is used. Applying a fast Fourier Transform (FFT) in the present data as a subroutine is used to estimate the density of electrons using the following equation: (Abdel-Latif 2016)

$$\rho(r) = \frac{1}{V}\sum_{\boldsymbol{H}} F(\boldsymbol{H}) exp\{-2\pi i(\boldsymbol{H}\cdot\boldsymbol{r})\}$$

Looking at this equation, it is quite clear that $\rho(r)$ depends on the following parameters: the unit cell volume (V), the reciprocal lattice vector (H), the position vector inside the unit cell (r), and the coefficients of the complex Fourier F(H), which are applied to implement the different types of Fourier syntheses. The units of $\rho(r)$ are the same of F(H) per volume. The electron density according to the calculations showed the low density in pure ytterbium manganites and it is increased in doped with both Nd and Sm, as shown in Fig. 2. The electron density in doped ytterbium manganites are closed to each other.

Raman scattering analysis

The understudy ytterbium manganites belongs to the hexagonal class structure of (P_{63cm}) space group representing six formula units with 38 Raman active phonon modes($9A_1$, $14E_1$, and $15E_2$) (Ghosh et al. 2009). According to Ghosh et al., the LO-TO splitting caused by the induced dipole moment are represented by A_1 and E_1 Raman modes. Raman spectra of $Yb_{0.8}Nd_{0.2}MnO_3$ and $Yb_{0.8}Sm_{0.2}MnO_3$ annealed at 850 °C are shown in Fig. 3. It is quite clear that the observed Raman modes in the under study samples correspond to hexagonal symmetry (A_1 = 102, E_2 = 216, E_2 = 450, A_1 = 620, and A_1 = 684 cm^{-1}). Comparing observed Raman shift with what was reported before (Iliev et al. 1997: Ghosh et al. 2009), it is found that there is consistency. This hexagonal structure consists of MnO_5 bipyramids, where the nonequivalent O(3) and O(4) atoms are forming a triangular base, while the O(1) and O(2) are located at the vertex (Iliev et al. 1997). The bonds originated from both manganese and oxygen atoms are as follows: Mn–O(1) and Mn–O(2) are

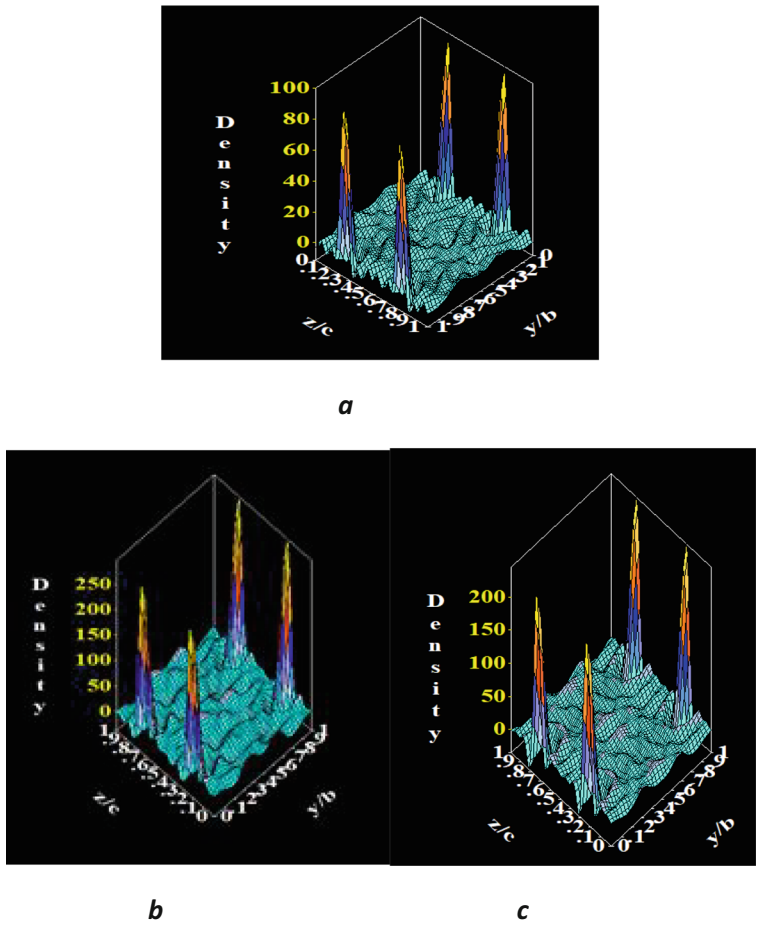

Fig. 2 Electron density map representation inside the unit cell. **a** $YbMnO_3$. **b** $Yb_{0.8}Nd_{0.2}MnO_3$. **c** $Yb_{0.8}Sm_{0.2}MnO_3$

slightly tilted with respect to the *c* axis. The rare earth atoms (Yb and Nd or Sm) are located between the bipyramidal layers taking into consideration that this structure consists of six formula units. The theoretical calculations of the group point analysis describing the phonon modes of hexagonal (*P*63*cm*) were listed in Table 2.

According to these results, the total group points are 60 modes *(10A_1, 5A_2, 10B_1, 5B_2, 15E_1, 15E_2),* including 38 Raman active modes. The A_1 and E_1 modes are termed as infrared active modes, while *the* A_2, B_1, and B_2 modes are termed as inactive or silent modes.

The experimentally Raman lines in measured spectra of $Yb_{0.8}Nd_{0.2}MnO_3$ are observed at 102, 131, 212, 460, 631, and 685 cm^{-1}, which correspond to E_2, A_1, E_2, A_1, E_1, and A_1, respectively. Spectral lines observed for $Yb_{0.8}Sm_{0.2}MnO_3$ are found at 101, 137, 217, 462, 630, and 687 cm^{-1}, which correspond to E_2, A_1, E_2, A_1, E_1, and A_1, respectively. Both A_1 and E_2 modes correspond to 102 and 131 cm^{-1} in $Yb_{0.8}Nd_{0.2}MnO_3$ as well as correspond to 101 and 137 cm^{-1} in $Yb_{0.8}Sm_{0.2}MnO_3$ are describing the motion of rare earth atoms Yb(1)/R(1) and Yb(2)/R(2) along with *c* axis and in ab plane, respectively. Oxygen atom motions in this rare earth manganites O(1) and O(2) are represented by $A_1 = 685$ cm^{-1}, while O(3) and O(4) are represented by $E_1 = 685$ cm^{-1}. Motion of manganese atom along z-axis is represented by $A_1 = 685$ cm^{-1}.

AC and DC electrical transport

The complex impedance measurements are strongly related to the microstructure of polycrystalline materials and depend on the grain size. The Complex impedance is not only affected by the morphology of the material but also by other parameters such as the conductivity type, frequency, and temperature. Looking at the conduction mechanism and electronic transfer that we can

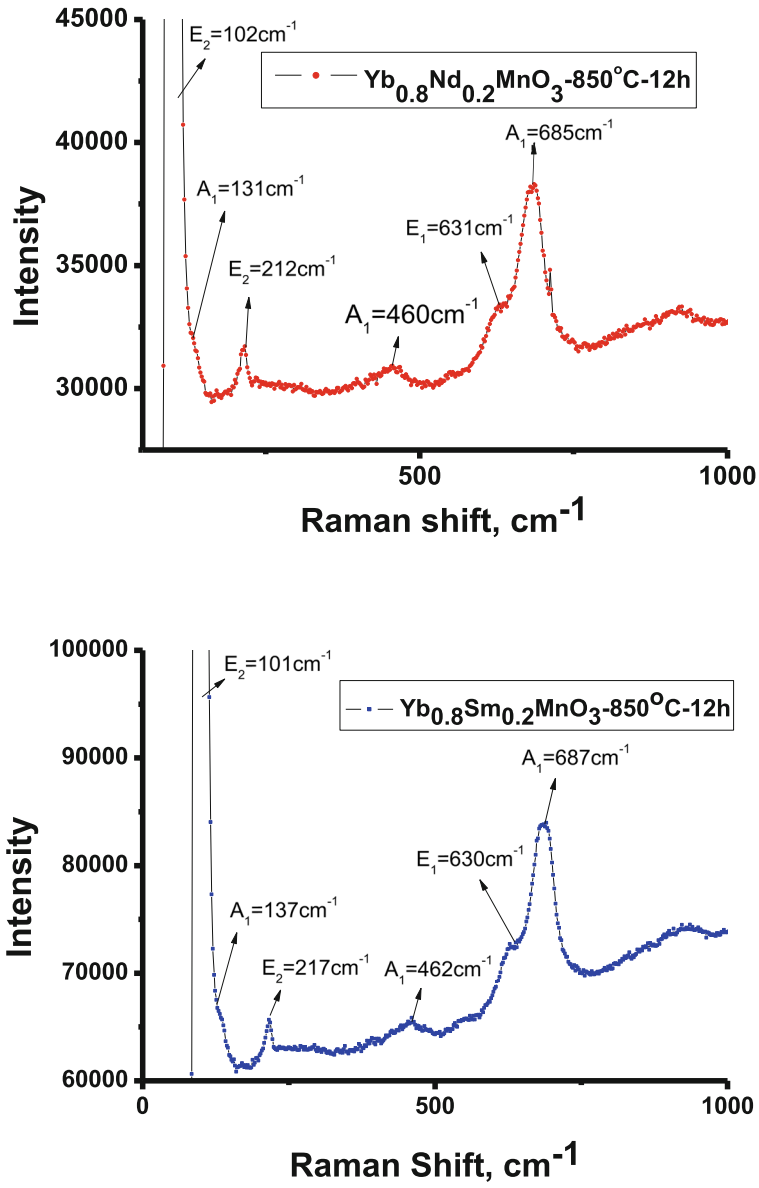

Fig. 3 Raman spectra of $Yb_{0.8}Nd_{0.2}MnO_3$ and $Yb_{0.8}Sm_{0.2}MnO_3$ annealed at 850 °C for 12 h

get from the complex impedance measurements where the electrical properties can be expressed on term parameters related to real and imaginary parts of impendence (Dadami et al. 2017).

$$Z^* = Z' + j\,Z\}$$

where $Z' = |Z| \cos\theta$ and $Z'' = |Z| \sin\theta$.

Impedance dependence on the frequency at different temperature of $Yb_{0.8}Nd_{0.2}MnO_3$ is shown in Fig. 4.

It is clear that the impedance has high value at low frequency and there is sharp decrease with increasing frequency. At high frequency, impedance is very low and almost independent on frequency.

The dielectric loss factor is a very important factor because it is affected by the following parameters: electric conduction and various polarization mechanisms (including dipole, electronic, ionic, and Maxwell–Wagner) (Komarov et al. 2005). As well-known before, the quantity used to describe dielectric properties is permittivity, which depends on the reflection of electromagnetic waves at interfaces and the attenuation of wave energy within materials. In terms of frequency dependence of the

Table 2 Positions, symmetry, and irreducible representations of hexagonal $Yb_{0.8}R_{0.2}MnO_3$ of space group *P*63*cm*

Atom	Wyckoff position	Symmetry	Irreducible representation
Yb(1)/R(1)	2(*a*)	$C_{3v}{}^{v}$	$A1 + B1 + E1 + E2$
Yb(1)/R(1)	4(*b*)	C_3	$A1 + A2 + B1 + B2 + 2E1 + 2E2$
Mn	6(*c*)	$C_s{}^{v}$	$2A1 + A2 + 2B1 + B2 + 3E1 + 3E2$
O(1)	6(*c*)	$C_s{}^{v}$	$2A1 + A2 + 2B1 + B2 + 3E1 + 3E2$
O(2)	6(*c*)	$C_s{}^{v}$	$2A1 + A2 + 2B1 + B2 + 3E1 + 3E2$
O(3)	2(*a*)	$C_{3v}{}^{v}$	$A1 + B1 + E1 + E2$
O(3)	4(*b*)	C_3	$A1 + A2 + B1 + B2 + 2E1 + 2E2$

Modes classification

$\Gamma_{Raman}\ 9A_1 + 14E_1 + 15E_2\ \Gamma_{IR}\ 9A_1 + 14E_1$

$\Gamma_{Silent}\ 5A_2 + 10B_1 + 5B_2\ \Gamma_{Acoustic}\ A_1 + E_1$

$A_1 = \alpha_{xx}{}^{z} + \alpha_{yy}{}^{z} + \alpha_{zz}{}^{z}$, $E_1 = \alpha_{xz}{}^{x}$, $\alpha_{yz}{}^{y}$, $E_2 = \alpha_{xx}\text{-}\alpha_{yy}$, a_{xy},

complex relative permittivity of any materials, one can express it in the following form:

$$\varepsilon^{*}=\varepsilon'+j\varepsilon'',$$

where ε′ and ε″ are the real permittivity (or relative dielectric constant) and imaginary permittivity (or dielectric loss), respectively. (Saleh 2019).

Both of the real and imaginary components of the dielectric as function of frequency can be deduced in terms of the impedance data according to the following formulas:

$$\varepsilon' = \frac{Z\}}{2\pi f C_0\left[(Z')^2+(Z\})^2\right]} \quad \varepsilon\} = \frac{Z'}{2\pi f C_0\left[(Z')^2+(Z\})^2\right]}.$$

where Z' and Z'' are real and imaginary components of the impedances, f is the frequency and C_o is the geometrical capacitance. The real part of dielectric, ε′, as a function of frequency at different temperatures is shown in Fig. 5. It is noted that there is a sharp decrease in the dielectric values at low frequencies then slight increase and after that almost independent on frequency. This behavior is the same for all temperatures. It is clear that there is a decrease with increasing frequency and at higher frequencies, permittivity is almost constant (dielectric dispersion). This dielectric dispersion can be explained in terms of nanostructure according to Maxwell and Wagner's bilayer model and Koops phenomenological theory (Bhasin et al. 2018).

The space charge polarization is clear in these materials due to heterogeneous dielectric nature of such materials and conducting grains generated. The dielectric loss tangent of any materials is an indication to the energy loss, which is given from the relation between

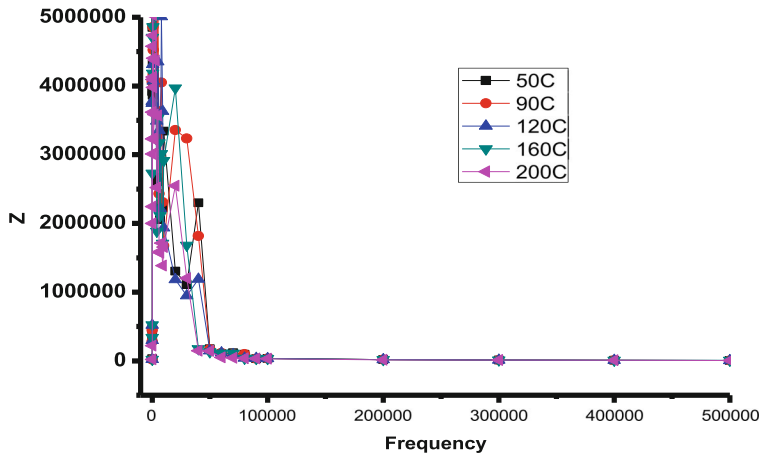

Fig. 4 Impedance variation as a function of frequency of $Yb_{0.8}Nd_{0.2}MnO_3$ at different temperatures

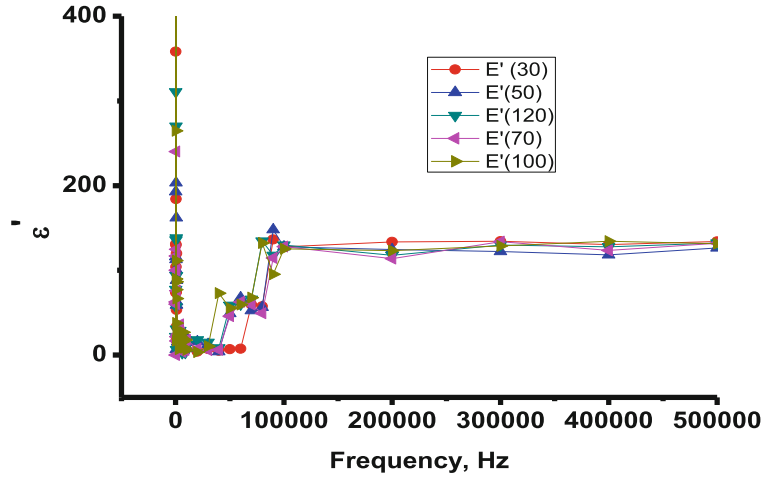

Fig. 5 The real part of dielectric as a function of frequency for $Yb_{0.8}Nd_{0.2}MnO_3$ at different temperatures

the real and imaginary dielectric permittivity according to the following formula:

$$D = \tan\delta = \varepsilon''/\varepsilon',$$

where δ is the phase difference between the induced current in the material and applied field (Varshney et al. 2018). According to our measurements tan δ decreases as a result of an increase of frequency. The sharp decrease in the value is observed at lower frequencies and at higher frequencies almost independent with frequency. The dielectric loss is mainly attributed to two parameters: resistive loss and relaxation loss. In the resistive loss, the mobility of charge has great effect, but in the relaxation loss, the dipoles effect is more pronounced (Sharma et al. 2014).

AC conductivity is one of the important parameters describing dielectric materials and dielectric properties where it is related to dielectric loss and dielectric constant. Moreover, it helps us to investigate the relaxation and concentration of charge carriers and this enables us to describe the nature of charge carriers. One can calculate it from the empirical equation given in reference to (Rehman et al. 2019)

$$\sigma_{ac} = 2\pi f \varepsilon_o \varepsilon\}$$

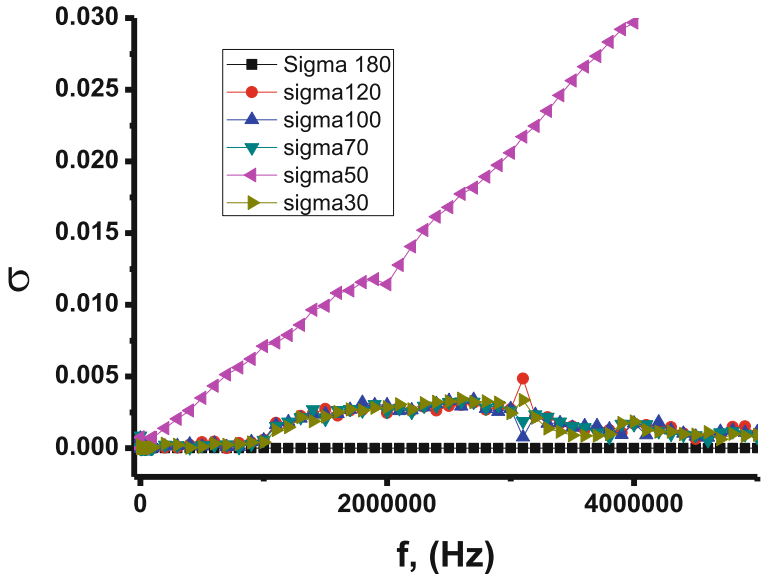

Fig. 6 AC conductivity for $Yb_{0.8}Nd_{0.2}MnO_3$ at different temperatures

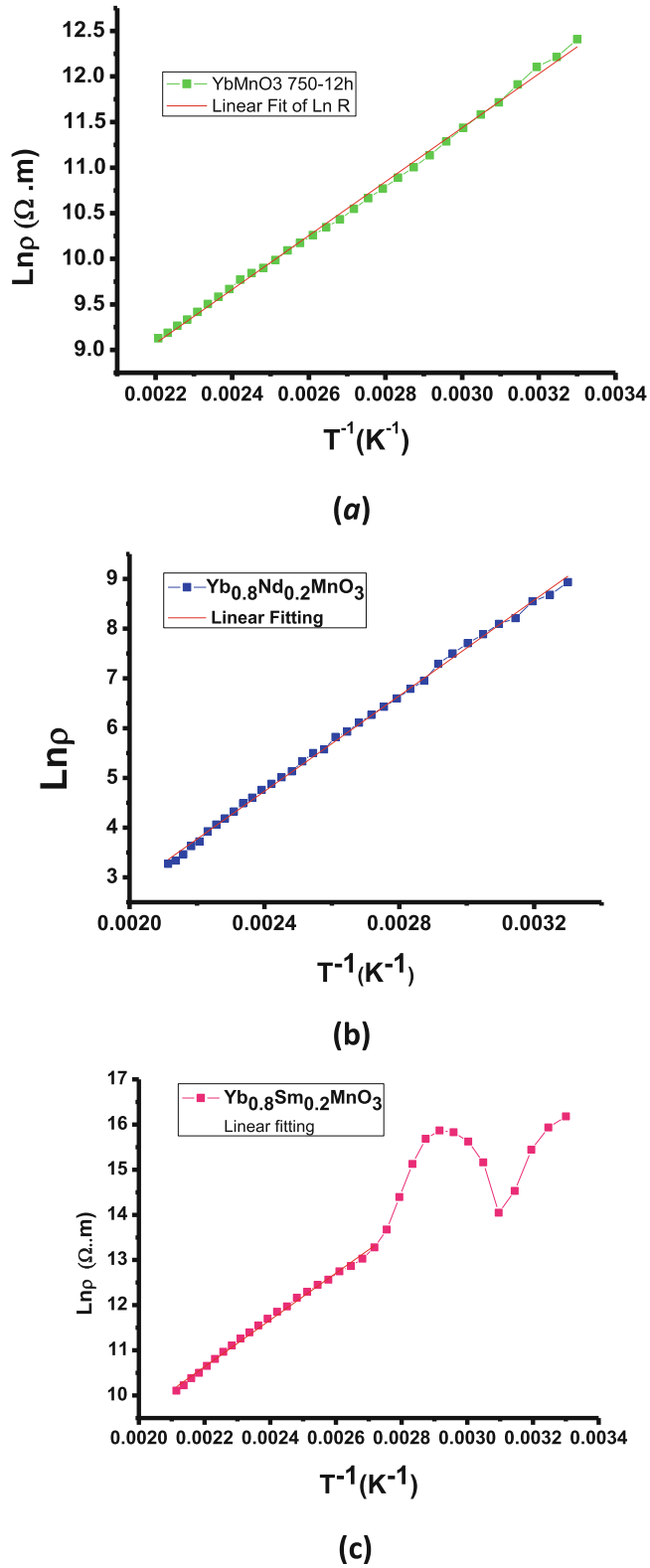

Fig. 7 DC resistivity variation as a function of temperature of undoped and doped ytterbium manganites

where *f* is termed as the frequency and ε_o is the dielectric permittivity in vacuum. The calculated AC conductivity for $Yb_{0.8}Nd_{0.2}MnO_3$ is shown in Fig. 6.

The increase in AC conductivity of $Yb_{0.8}Nd_{0.2}MnO_3$ with frequency increase is shown in Fig. 6 enhancing the hopping mechanism of charge carriers transfer (Rajwali et al. 2015). This increase of AC conductivity with increasing frequency may be attributed to series resistance effect as reported by (Khan et al. 2016). As it is well-known, AC conductivity of any materials is strongly correlated to the hopping of weakly bound charge carriers found in these materials (Ahmad et al. 2018).

To define the general behavior of electrical properties from the resistivity-temperature dependence measurements and to get more information about current transport mechanisms in the present compounds, the DC resistivity variation as a function of temperature measurements of undoped and doped ytterbium manganites are carried out and are shown in Fig. 6. The relation between resistivity and temperature is exponential as given in the equation below, and it may be attributed to the semiconducting characteristics of these under study materials at the temperature range from room temperature up to 473 k (Abdel-Latif et al. 2018a, b).

$$\rho = \rho_0 e^{\frac{E_a}{KT}}$$

The calculated activation energy listed in Table 1 for all samples confirms the semiconducting behavior. The values of E_a deduced for YbMnO3 annealed at 750 °C and doped ytterbium manganites with Sm and Nd annealed at 850 °C are given in Table 1. There is an increase in the activation energy because of doping. The linear dependent in $YbMnO_3$ and $Yb_{0.8}Nd_{0.2}MnO_3$ are found, while for $Yb_{0.8}Sm_{0.2}MnO_3$ there is peak that appeared at 343 K and this may be attributed to some magnetic ordering. The significant difference in activation energy between pure and doped ytterbium manganites is found because of the remarkable difference in the crystalline size (Fig. 7).

Conclusions

- The hexagonal structure system of space group *P63cm does not change because of* samarium and neodymium doping in ytterbium manganites.
- The crystalline size observed for pure ytterbium manganite is 67 nm and it increased with doping.
- All samples showed the semiconducting behavior except samarium-doped ytterbium manganite, where there is a peak at 343 K that may be attributed to magnetic ordering.
- The increase in AC conductivity is found with frequency increase for $Yb_{0.8}Nd_{0.2}MnO_3$ sample enhancing the hopping mechanism of charge carriers transfer.

Funding information The present research is supported by the Deanship of Scientific Research fund program in Najran University. The author is grateful for this financial support NU/ESCI/16/063 given to him in the frame of the local scientific research program support.

Compliance with ethical standards

Conflict of interest The author declares that he has no conflict of interest.

References

Abdel-Latif IA (2011) Study on the effect of particle size of strontium - ytterbium manganites on some physical properties. AIP Conf Proc 1370:108–115. https://doi.org/10.1063/1.3638090

Abdel-Latif IA (2016) Study on structure, electrical and dielectric properties of $Eu_{0.65}Sr_{0.35}Fe_{0.3}Mn_{0.7}O_3$. IOP Conf Series: Mater Sci Eng 146:012003. https://doi.org/10.1088/1757-899X/146/1/012003

Abdel-Latif IA et al (2008) The influence of tilt angle on the CMR in $Sm_{0.6}Sr_{0.4}MnO_3$. J. Alloys Compd 452:245–248. https://doi.org/10.1016/j.jallcom.2007.07.022

Abdel-Latif IA et al (2015) Synthesis of novel perovskite crystal structure phase of strontium doped rare earth Manganites using sol gel method. J Magn Magn Mater 393:233–238. https://doi.org/10.1016/j.jmmm.2015.05.078

Abdel-Latif IA et al (2016) Electrical and magnetic transport in strontium doped europium Ferrimanganites. J Magn Magn Mater 420:363–370. https://doi.org/10.1016/j.jmmm.2016.07.016

Abdel-Latif IA et al (2017) Impact of the annealing temperature on Perovskite strontium doped neodymium Manganites Nanocomposites and their Photocatalytic performances. J Taiwan Inst Chem Eng 75:174–182. https://doi.org/10.1016/j.jtice.2017.03.030

Abdel-Latif IA et al (2018a) Neodymium cobalt oxide as a chemical sensor. Results Phys 8:578–583. https://doi.org/10.1016/j.rinp.2017.12.079

Abdel-Latif IA et al (2018b) Magnetocaloric effect, electric, and dielectric properties of $Nd_{0.6}Sr_{0.4}Mn_xCo_{1-x}O_3$ composites. J Magn Magn Mater 457:126–134. https://doi.org/10.1016/j.jmmm.2018.02.087

Abdel-Latif IA, al-Hajji LA, Faisal M, Ismail AA (2019) Doping strontium into neodymium Manganites Nanocomposites for enhanced visible light driven Photocatalysis. Sci Rep 9: 13932. https://doi.org/10.1038/s41598-019-50393-9

Ahmad N, Khan S, Ansari MMN (2018) Microstructural, optical and electrical transport properties of cd-doped SnO_2 nanoparticles. Mater Res Express 5(3):035045

Ayas AO et al (2017) Room temperature magnetocaloric effect in $Pr_{1.75}Sr_{1.25}Mn_2O_7$ double-layered perovskite manganite system. Philos Mag. https://doi.org/10.1080/14786435.2017.1279363

Bashkirov S et al (2003) Crystal structure, electric and magnetic properties of Ferrimanganite $NdFe_xMn_{1-x}O_3$. Bull Russian Acad Sci Phys (Izvestiya Akademii Nauk Ser Fizicheskaya) 67:1165–1169

Bashkirov S et al (2005) Mössbauer effect and electrical conductivity studies of $SmFe_xMn_{1-x}O_3$ (x=0.7, 0.8 and 0.9). J Alloys Compd 387:70–73. https://doi.org/10.1016/j.jallcom.2004.06.070

Bettaibi A, M'nassri R, Selmi A et al (2016) Effect of small quantity of chromium on the electrical, magnetic and magnetocaloric properties of $Pr_{0.7}Ca_{0.3}Mn_{0.98}Cr_{0.02}O_3$ manganite. Appl Phys A Mater Sci Process 122:232. https://doi.org/10.1007/s00339-016-9780-9

Bhasin T et al (2018) Crystal structure, dielectric, magnetic and magnetoelectric properties of $xNiFe_2O_4$-(1-x)$Na_{0.5}Bi_{0.5}TiO_3$ composites. J Alloys Compd 748:1022–1030. https://doi.org/10.1016/j.jallcom.2018.03.219

Bouziane KA et al (2005) Electronic and magnetic properties of SmFe1-xMnxO3 orthoferrites (x = 0.1, 0.2 and 0.3). *J Appl Phys* 97:10A504. https://doi.org/10.1063/1.1851406

Bykov EO et al (2019) Structural and magnetic properties of Yb1−xSrxMnO3. Ceram Int 45:10286–10294. https://doi.org/10.1016/j.ceramint.2019.02.083

Chandran K, Lekshmi PN, Santhosh PN (2019) High temperature spin reorientation, magnetization reversal and magnetocaloric effect in 50% Mn substituted polycrystalline $ErFeO_3$. J Solid State Chem 279:120910. https://doi.org/10.1016/j.jssc.2019.120910

Cherif R et al (2014) Magnetic and magnetocaloric properties of $La_{0.6}Pr_{0.1}Sr_{0.3}Mn_{1-x}Fe_xO_3$ ($0 \le x \le 0.3$) manganites. J Solid State Chem 215:271–276. https://doi.org/10.1016/j.jssc.2014.04.004

Dadami ST et al (2017) Impedance spectroscopy studies on PbFe 0.5 Nb 0.5 O 3 –BiFeO 3 Multiferroic solid solution. Ceram Int 43:16684–16692. https://doi.org/10.1016/j.ceramint.2017.09.059

Das H, Wysocki AL, Geng Y, Wu W, Fennie CJ (2014) Bulk magnetoelectricity in the hexagonal manganites and ferrites. Nat Commun 5:2998–2911. https://doi.org/10.1038/ncomms3998

Elghoul A et al (2018) Rare earth effect on structural, magnetic and magnetocaloric properties of $La_{0.75}Ln_{0.05}Sr_{0.2}MnO_3$ manganites. Ceram Int 44(11):12723–12730. https://doi.org/10.1016/j.ceramint.2018.04.075

Fabreges X et al (2009) Spin-lattice coupling, frustration, and magnetic order in multiferroic RMnO3. Phys Rev Lett 103(6):067204

Gamzatov AG, Aliev AM, Kaul AR (2017) Magnetocaloric effect in $La_{1-x}K_xMnO_3$ (x = 0.11, 0.13, 0.15) composite structures in magnetic fields up to 80 kOe. J Alloys Compd 710:292–296. https://doi.org/10.1016/j.jallcom.2017.03.300

Ghosh A et al (2009) A Raman study of multiferroic LuMnO3. Solid State Sci 11(9):1639–1642. https://doi.org/10.1016/j.solidstatesciences.2009.06.002

Iliev MN et al (1997) Raman- and infrared-active phonons in hexagonal $YMnO_3$: experiment and lattice-dynamical calculations. Phys Rev B 56:2488–2494. https://doi.org/10.1103/PhysRevB.56.2488

Iqbal MJ, Ahmad Z, Meydan T, Melikhov Y (2012) Physical, electrical and magnetic properties of nano-sized co-Cr substituted magnesium ferrites. J Appl Phys 111:033906. https://doi.org/10.1063/1.3676438

Iqbal M, Khan MN, Khan AA et al (2017) Structure and charge transport mechanism in hydrothermally synthesized ($La_{0.5}Ba_{0.5}MnO_3$) cubic perovskite manganite. J Mater Sci Mater Electron 28:15065. https://doi.org/10.1007/s10854-017-7381-9

Kanhere P, Chen Z (2014) A review on visible light active Perovskite-based Photocatalysts. Molecules 19(12):19995–20022. https://doi.org/10.3390/molecules191219995

Khan R et al (2016) Effect of annealing on structural, dielectric, transport and magnetic properties of (Zn, Co) co-doped SnO_2 nanoparticles. J Mater Sci Mater Electron 27(4):4003–4010. https://doi.org/10.1007/s10854-015-4254-y

Komarov V, Wang S, Tang J (2005) Permittivity and measurements. Encyclopedia of RF and microwave engineering, edited by Kai Chang ISBN 0-471-27053-9 *r* : 3693-3711 John Wiley & Sons, Inc

Lee et al (2005) Direct observation of a coupling between spin, lattice, and electric dipole moment in multiferroic YMnO3. Phys Rev B 71:180413R. https://doi.org/10.1103/PhysRevB.71.180413

Lee S, Pirogov A, Kang M, Jang KH, Yonemura M, Kamiyama T, Cheong SW, Gozzo F, Shin N, Kimura H, Noda Y, Park JG (2008) Giant magneto-elastic coupling in multiferroic hexagonal manganites. Nature 451:805–809. https://doi.org/10.1038/nature06507

Mahato Dev K, Sujoy S, Sinha TP (2016) Structural studies and impedance spectroscopy of sol–gel derived $Bi_{0.9}Pr_{0.1}FeO_3$ nanoceramics. J Phys Chem Solids 92:45–52

Maignan A et al (1997) Solid State Commun 101(4):277–281

Markovich V, Puzniak R, Fita I et al (2013) J Nanopart Res 15: 1862. https://doi.org/10.1007/s11051-013-1862-4

Naseem S et al (2018) Dielectric response and room temperature ferromagnetism in Cr doped anatase TiO_2 nanoparticles. J Magn Magn Mater 447:155–166. https://doi.org/10.1016/j.jmmm.2017.09.051

Parfenov VV et al (2003) Transfer phenomena in $Nd_{0.65}Sr_{0.35}Mn_{1-x}Fe_xO_3$ ferrimanganites. Russ Phys J 46(10):979–980

Parfenov VV et al (2007) On the structure and transport mechanism of $Nd_{0.65}Sr_{0.35}Mn_{1-X}Fe_XO_3$ solid solution (X=0, 0.2, 0.4, 0.8). Arab J Nucl Sc Appl 40(1):167–174

Rajwali K, et al., (2015) Dielectric and magnetic properties of (Zn, co) co-doped SnO_2 nanoparticles. Chinese Phys. B 24 (12): 127803 https://doi.org/10.1088/1674-1056/24/12/127803

Ramesh R, Spaldin N (2007) Multiferroics: progress and prospects in thin films. Nat Mater 6:21–29. https://doi.org/10.1038/nmat1805

Rehman F et al (2019) Dielectric relaxation and electrical properties of $Bi_{2.5}Nd_{0.5}Nb_{1.5}Fe_{0.5}O_9$ ceramics. Mater Chem Phys 226:100–105. https://doi.org/10.1016/j.matchemphys.2019.01.025

Ritter CA (1996) New monoclinic perovskite allotype in $Pr_{0.6}Sr_{0.4}MnO_3$. J Solid State Chem 127:276–282. https://doi.org/10.1006/jssc.1996.0384

Rodriguez-Carvajal (1993) Recent advances in magnetic structure determination by neutron powder diffraction. Physica B 192: 55–69. https://doi.org/10.1016/0921-4526(93)90108-I

Rossli R et al (2005) Spin fluctuations in the stacked-triangular antiferromagnet $YMnO_3$. JETP Lett 81(6):287–291. https://doi.org/10.1134/1.1931017

Rousseau DL, Bauman RP, Porto SPS (1981) J Raman Spectrosc 10:253–290. https://doi.org/10.1002/jrs.1250100152

Salama H et al (2008) A Mossbauer spectroscopy investigation of h-$YbMnO_3$. J Phys Condens Matter 20:255213–225219. https://doi.org/10.1088/0953-8984/20/25/255213

Saleh SA (2019) Study of microstructural, electrical and dielectric properties of $La_{0.9}Pb_{0.1}MnO_3$ and $La_{0.8}Y_{0.1}Pb_{0.1}MnO_3$ ceramics. Sci Rev 5:33–44. https://doi.org/10.32861/sr.52.33.44

Sharma HB et al (2014) Ac electrical conductivity and magnetic properties of $BiFeO_3$–$CoFe_2O_4$ nanocomposites. J Alloys Compd 599:32–39. https://doi.org/10.1016/j.jallcom.2014.02.024

Shuk P, Guth U (1995) Mixed conductive electrode materials for sensors and SOFC. Ionics 1:106–111. https://doi.org/10.1007/BF02388666

Shuk P et al (1993) Electrodes for oxygen sensors based on rate earth manganites or cabaltites. Sensors Actuators B *15–16*: 401–405. https://doi.org/10.1016/0925-4005(93)85218-Y

Smolenskii GA, Chupis IE (1981) Ferroelectromagnets. Sov Physics-Uspekhi 25:475. https://doi.org/10.1070/PU1982v025n07ABEH004570

Talbayev D et al (2008) Magnetic exchange interaction between rare-earth and Mn ions in multiferroic hexagonal manganites. Phys Rev Lett 101:247601

Tokunaga Y, Lottermoser T, Lee Y, Kumai R, Uchida M, Arima T, Tokura Y (2006) Rotation of orbital stripes and the consequent charge-polarized state in bilayer manganites. Nat Mater 5:973–941. https://doi.org/10.1038/nmat1773

Van Aken BB, Palstra TTM, Filippetti A, Spaldin NA (2004) The origin of ferroelectricity in magnetoelectric YMnO3. Nat Mater 3(3):164. https://doi.org/10.1038/nmat1080

Varshney M et al (2018) Electronic structure and dielectric properties of ZrO_2-CeO_2 mixed oxides. J Phys Chem Solids 119: 242–250. https://doi.org/10.1016/j.jpcs.2018.04.007

Wang YT, Luo CW, Kobayashi T (2013) Understanding multiferroic hexagonal manganites by static and ultrafast optical spectroscopy. Adv Condens Matter Phys. https://doi.org/10.1155/2013/104806

Yousif AA et al (2011) Study on Mossbauer and magnetic properties of strontium doped neodymium ferrimanganites perovskite-like structure. AIP Conf Proc 1370:103–107. https://doi.org/10.1063/1.3638089

Zhang B et al (2016) Effects of strain relaxation in $Pr_{0.67}Sr_{0.33}MnO_3$ films probed by polarization dependent X-ray absorption near edge structure. Sci Rep 6:19886. https://doi.org/10.1038/srep19886

Zhou J-S, Goodenough JB, Gallardo-Amores JM, Moran E, Alario-Franco MA, Caudillo R (2006) Hexagonal versus perovskite phase of manganite RMnO3 (R=Y, Ho, Er, Tm, Yb, Lu). Phys Rev B 74(1):014422. https://doi.org/10.1103/PhysRevB.74.014422